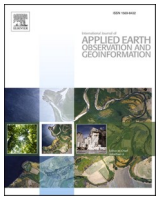
International Journal of Applied Earth Observation and Geoinformation 154 (2026) 105609



Contents lists available at ScienceDirect

International Journal of Applied Earth Observation and Geoinformation

journal homepage: www.elsevier.com/locate/jag



Reference-anchored envelope modelling for predicting tree mortality hotspots driven by drought

Filippos Eliades [a,b,*], Dimitrios Sarris [c,d], Felix Bachofer [e], Silas Michaelides [b], Chris Danezis [a,b], Diofantos Hadjimitsis [a,b]

[a] Department of Civil Engineering and Geomatics, Remote Sensing and GeoEnvironment Lab, Cyprus University of Technology, Limassol, Cyprus
[b] Eratosthenes Centre of Excellence, Limassol, Cyprus
[c] KES Research Centre, Nicosia, Cyprus
[d] KES College, Nicosia, Cyprus
[e] German Aerospace Center (DLR), Earth Observation Center (EOC), Wessling, Germany

ARTICLE INFO

Keywords:
Forest decline
Climate change
Remote sensing
Mortality hotspots
Drought-driven tree mortality

ABSTRACT

Predicting tree mortality hotspots driven by drought remains challenging, since vulnerability to drought is strongly influenced by climate, landform, and substrate. We propose a novel reference-anchored, quantile-envelope susceptibility model-implemented through a reproducible workflow- that exports mortality-resemblance (high-risk) environments from three confirmed tree-mortality footprints (training AOIs), based on semi-arid conifer and evergreen sclerophyllous forests in Cyprus, to produce wide screening layers. The approach combines (i) physiographic similarity derived from AOI-calibrated envelopes for slope, multi-scale topographic position and curvature (broad quantiles; majority-rule), (ii) exposure constraints via circular aspect windows, warm-season solar loading (April-September) and substrate (lithology) filtering, (iii) a drought severity gate (SPEI-12 (Standardized Precipitation-Evapotranspiration Index-12) $\leq$ -1.4), and (iv) Landsat event-year spectral collapse relative to a fixed 3-year pre-event baseline, coupled with a year + 1 persistence rule to suppress transient stress. Our within-AOI evaluation (forest-only) showed substantial representativeness (coverage 70.49–85.35%), while recovering most reference mortality pixels (recall 67.62–100%). In 2025, two independent mortality sites were identified in Cyprus, coinciding with exceptional drought (SPEI < -2) and a sharp decline in the Normalized Burn Ratio (NBR) consistent with foliage browning, and occurring within high-risk zones as mapped in the final risk map. As a plausibility check, both 2025 sites fell within pre-mapped high-risk zones, with 83.50% and 82.69% of their forested area exceeding HEAT $\geq$ 0.60 and mean risk scores of 84.91% and 75.55%, respectively. With 18.88% of Cyprus's total forest flagged as high-risk, the probability of this co-occurrence being random is p $\approx$ 0.036 (binomial test). Anchoring calibration to local mortality footprints makes the approach readily transferable to other regions with documented events.

1. Introduction

Climate warming is intensifying drought and heat extremes across semi-arid and Mediterranean ecosystems, increasing the likelihood that episodic climatic shocks translate into abrupt forest decline and tree mortality (Allen et al., 2010; Carnicer et al., 2011; Sánchez-Salguero and Camarero, 2020). Mortality in these regions typically results from interactions between climate anomalies and local controls on water availability and energy balance, including topography (Paz-Kagan et al., 2017; Sang et al., 2024), geological substrate (Nardini et al., 2024; Schwantes et al., 2018), and solar radiation exposure (Guan et al., 2021; Ma et al., 2023), often in combination (Dorman et al., 2015). Consequently, neighboring stands can follow contrasting trajectories during the same event, from transient stress to persistent canopy loss, depending on landscape position (Sarris and Christodoulakis, 2024).

Remote sensing provides multi-decadal records of canopy condition through vegetation indicators sensitive to greenness and stress-related spectral properties (Banskota et al., 2014; De Marzo et al., 2021; Eliades et al., 2024; Tucker, 1979). However, converting indicator anomalies into actionable mortality-risk products remains challenging

* Corresponding author.
E-mail address: filippos.eliades@gmail.com (F. Eliades).

https://doi.org/10.1016/j.jag.2026.105609
Received 3 March 2026; Received in revised form 13 September 2026; Accepted 19 September 2026
Available online 22 September 2026
1569-8432/© 2026 The Author(s). Published by Elsevier B.V. This is an open access article under the CC BY license (http://creativecommons.org/licenses/by/4.0/).

because different disturbance pathways (e.g., drought, fire, pests, management) can produce similar spectral signals (Rodríguez Paulino et al., 2024), and because recurrence of mortality is strongly mediated by landscape structure, runoff potential, soil-moisture redistribution, and microclimatic exposure rather than climate forcing alone (Breshears et al., 2005; Gustafson and Sturtevant, 2013). This limits spatial prioritization for monitoring and intervention across heterogeneous forest domains.

An environmental-envelope strategy can complement anomaly detection by delineating *mortality-prone* settings based on the physiographic and hydroclimatic conditions observed in confirmed mortality footprints (Mbogga et al., 2010; Wiens et al., 2009). This yields a "resemblance-zone" layer: areas environmentally analogous to known mortality sites that also satisfy event-consistent evidence of stress and post-event persistence. Such layers are not a substitute for field validation, but a screening product to prioritize surveillance and ground checks toward the most plausible high-risk environments.

A key challenge is transferability: Areas of interest (AOIs)[1] with confirmed mortality, often differ in morphology, substrate, and exposure, so thresholds calibrated at one site may fail elsewhere (Regos et al., 2019; Yates et al., 2018). Robust operational deployment, therefore, requires *anchoring* to observed mortality environments while *relaxing* overly strong assumptions to support generalization across unfamiliar terrain and event contexts. Despite these advances, no operational framework exists that simultaneously anchors mortality signatures to confirmed footprints, accounts for physiographic landscape controls, and transfers predictions across contrasting species and terrain settings within a reproducible cloud-based workflow.

In this study, we develop and test a reference-anchored workflow/model in Google Earth Engine (GEE) that delineates mortality-like "high-risk areas" by integrating AOI-derived physiographic similarity constraints, Landsat-based event-year spectral decline referenced to a multi-year pre-event baseline, and a post-event persistence requirement, applied within a national forest mask. We demonstrate the approach in Cyprus using three AOIs with confirmed forest mortality spanning contrasting landscape settings (Akamas, Stavrovouni and Machairas) and two major drought-related mortality episodes (2008 and 2016). Although the AOIs are dominated by different tree species, the composite map is intended as a landscape-scale screening product for drought-related mortality risk rather than a species-specific mortality model.

The objective is to present a reference-anchored envelope-based susceptibility model implemented in GEE that transfers a mortality "signature" from confirmed mortality footprints to a broader forest domain.

This study addresses three research questions:

1. To what extent can signatures from confirmed mortality events predict near-future high-risk areas beyond the AOIs?

2. What is the optimal tradeoff between sensitivity and specificity for the majority rule?

3. Which predictors contribute most to performance, and which are weak or site-dependent?

To support practical use, we frame evaluation around two complementary measures-within-AOI forest representativeness (spatial coverage) and sensitivity to confirmed mortality pixels (recall), and propose a conservative reliability gate: a map should exceed 60% in both metrics before being treated as an actionable high-risk product for management-oriented screening.

[1] For a complete explanation of all the acronyms and abbreviations, the reader is referred to the Appendix.

2. Methodology

2.1. Study areas

The analysis focused on three forested areas in Cyprus: Akamas (*J. phoenicea*), Stavrovouni (*P. brutia*), and Machairas (*Q. alnifolia*). The sites span contrasting biophysical settings (elevation, slope, aspect, and geological substrate; mapped lithology) and include documented episodes of tree mortality or severe canopy decline during the study period. For each area, summary terrain metrics (elevation, slope, aspect, terrain position, and curvature) were computed to characterize local conditions and support the derivation of environmental thresholds. The three sites differ markedly in elevation (Stavrovouni: ~270–316 m a.s.l.; Akamas: low-to-mid elevation; Machairas: 1,005–1,267 m a.s.l.), slope (gentle at Stavrovouni 1-26°; moderate at Akamas 2-27°; steep at Machairas 16-41°), aspect (northeast-facing at Stavrovouni; south-southeast at Akamas; east-northeast at Machairas), geological substrate (biocalcarenites at Stavrovouni; ophiolitic diabase at Akamas; greywacke/marls at Machairas), and dominant tree species (*P. brutia*, *J. phoenicea*, and *Q. alnifolia*, respectively) (Table 1).

2.2. Data sources and preprocessing

2.2.1. Remote sensing data and preprocessing

We used annual time series (1984–2022) of vegetation and structure/severity indicators derived from medium-resolution multispectral Landsat imagery. Annual mean NDVI (Normalized Difference Vegetation Index) was calculated for Machairas, while annual mean NBR (Normalized Burn Ratio) was calculated for Akamas and Stavrovouni (Eliades et al., 2026). For each protected area and year, we merged Landsat 5 TM, Landsat 7 ETM+, Landsat 8 OLI, and Landsat 9 OLI-2 Collection 2 Level-2 surface reflectance data, applied Collection 2 radiometric scaling to optical bands, harmonized band names across sensors, and masked clouds/cloud shadows using the `QA_PIXEL` bitmask (cloud bit 3; cloud-shadow bit 4). Cloud-free observations within each calendar year were aggregated into an annual per-pixel mean composite, and the spatial mean index value within each AOI was extracted using a mean reducer at 30 m resolution (scale = 30 m).

Table 1
Original topographic, solar and drought thresholds defining mortality signatures in the three study areas.

Category	Variable	Area 1	Area 2	Area 3
Remote Sensing Indicator	`Average_NBR`	−35.8	−35.8	
Remote Sensing Indicator	`Average_NDVI`			−18.9
Drought (SPEI)	`SPEI12m_max`	−1.4	−1.4	−1.4
Solar exposure	`SOLAR_IDX_min`	0.70	0.87	0.66
Topography – TPI1000	`TPI1000_min`	−62.33	−26.20	−138.13
Topography – TPI1000	`TPI1000_max`	44.46	20.72	123.61
Topography – TPI300	`TPI300_min`	−44.47	–22.19	−93.33
Topography – TPI300	`TPI300_max`	37.08	18.21	91.86
Aspect	`aspect_center_deg`	144.50	21.55	74.23
Aspect	`aspect_halfwidth_deg`	53.56	58.60	24.91
Curvature	`curv8_min`	−100.00	−100.00	−100.00
Curvature	`curv8_max`	66.66	69.56	100.00
Slope	`slope_min_deg`	2.00	1.00	16.00
Slope	`slope_max_deg`	27.00	26.00	41.00
Geology	`geology_codes`	[34, 37, 10]	[5]	[34]

2.2.2. Drought index

To characterize interannual drought variability, we used the SPEI aggregated over a 12-month time scale (SPEI-12) (Vicente-Serrano et al., 2010). For each protected area, we extracted annual SPEI-12 values (CSIC/SPEI/2_10) for the same period as the remote-sensing data and computed a continuous time series of mean annual drought conditions. Input climate data (precipitation and temperature) used to derive SPEI were obtained from the Cyprus Department of Meteorology. These series were later used to constrain "where-else" predictions to years and locations experiencing comparable drought stress to the reference mortality events.

2.3. Definition of reference mortality signatures

For each case-study area, we defined one "authentic" mortality event year based on documented episodes of extensive canopy decline: 2016 for Akamas (NBR), 2008 for Stavrovouni (NBR), and 2008 for Machairas (NDVI). Using annual mean Landsat indicator time series, we quantified a reference-anchored mortality signature relative to a three-year pre-event baseline, selected to reduce interannual noise while avoiding longer windows that may blend distinct hydroclimatic regimes or longer-term trends. Baseline conditions were computed as the mean annual NDVI/NBR over (event year −3) to (event year −1) (see Julio Camarero et al., 2018). Event impact was expressed as (i) Δ (event − baseline) and (ii) `drop_pct = (delta / baseline) × 100`. To capture short-term persistence, we computed an analogous post-event Δ for event year + 1 relative to the same pre-event baseline (post + 1 − baseline), representing continued degradation (Hawbaker et al., 2017). All baseline and change metrics were calculated as mean values within the mapped confirmed mortality footprints (forest mortality patches) and used to define the "authentic" reference signature for each area (baseline, event `drop_pct`, and post-event persistence Δ) together with the corresponding indicator (NDVI or NBR).

Baseline length can influence Δ under inter-annual variability. However, in our framework, the baseline is part of a reference-anchored signature and is re-estimated together with the derived thresholds when the baseline window is changed. In addition, the final resemblance masks are constrained by multiple independent filters (e.g., topography, SPEI/seasonal drought constraint, solar exposure, geological substrate (lithology), and post-event persistence), which.

2.4. Topographic covariates associated with canopy mortality

These covariates describe broad-scale landscape position (elevation, topographic position, and curvature) and local energy/moisture environments (slope, aspect, and potential solar loading). Slope governs surface runoff rates and erosion potential (Schwantes et al., 2018), TPI distinguishes water-accumulating valley positions from moisture-limited ridges (Huesca et al., 2021), and curvature controls lateral water redistribution across the hillslope (McLaughlin et al., 2020). Together, these terrain attributes serve as proxies for the ecohydrological processes that mediate stand-level soil moisture availability and, ultimately, vulnerability to drought-induced mortality (Paz-Kagan et al., 2017; Dorman et al., 2015).

2.4.1. Topographic position index

TPI was computed as the difference between focal-cell elevation and neighborhood mean elevation at two spatial scales: a local TPI using a 300-m neighborhood (`TPI300`) and a *meso*-scale TPI using a 1,000-m neighborhood (`TPI1000`). Positive TPI values denote terrain higher than its surroundings (ridges/upper slopes), values near zero indicate mid-slope positions, and negative values indicate depressions/valley bottoms; we used TPI300 and TPI1000 to assess how local versus *meso*-scale topographic position modulates stand-level water-stress exposure and associated tree mortality (Huesca et al., 2021).

2.4.2. Curvature metric

Curvature was quantified using an eight-neighbor Laplacian operator applied to the DEM (`curv8`). Positive `curv8` values therefore, correspond to locally convex terrain (e.g., spurs and crests), whereas negative values indicate locally concave terrain (e.g., hollows, small drainage lines or toe slopes) that are more likely to concentrate water and cold air. Values close to zero represent relatively planar surfaces (Salekin et al., 2019).

2.4.3. Elevation

We extracted elevation from the COPERNICUS/DEM/GLO30 (Copernicus Data Space Ecosystem, 2026) and summarized its distribution within the canopy-mortality AOIs. Elevation was treated as a continuous proxy for macroclimatic forcing and broad gradients in soil development and vegetation composition (Gea-Izquierdo et al., 2014). For each study area, we reported the minimum, maximum and standard deviation of elevation for pixels within mapped mortality patches, using these statistics to describe the typical altitudinal band and, where relevant, to define optional elevation envelopes (e.g., mean ± 1 SD) for extrapolation.

2.4.4. Slope

Local slope was derived from the same DEM (degrees). For each event we summarized slope within the mortality AOI by mean, standard deviation and range and used these summaries to define slope envelopes (e.g., mean ± 1 SD) (Schwartz et al., 2020).

2.4.5. Aspect

Aspect was computed from the DEM (0-360°, 0° = north). We converted aspect to eastness and northness and used these to compute circular statistics (mean direction and dispersion) (Amatulli et al., 2018). These parameters were translated into aspect windows (e.g., mean ± one circular standard deviation) and used as part of the multi-criteria "likeness" masks.

2.4.6. Potential solar exposure

We derived a dimensionless solar exposure index (`SOLAR_IDX`) from latitude, slope and aspect using the cosine of the incidence angle, truncated to [0,1]. Monthly `SOLAR_IDX` images were calculated for 1992–2020 and aggregated to seasonal means for April-September (Baguskas et al., 2014).

2.4.7. Geological substrate and soil-forming environment

We intersected each protected area with a national geological map and treated mapped geological substrate (bedrock lithologies and mapped surficial/unconsolidated deposits) as a proxy for parent material and soil-forming environment (McLaughlin et al., 2020). Vector polygons were recoded into a categorical "substrate (lithology) code" layer (see Supplementary Table S2). For each event, we identified the dominant substrate underlying mortality patches (greatest areal share). Geological data were obtained from the Geological Survey Department of Cyprus (Camera et al., 2017).

2.5. Deriving mortality signatures and thresholds using GEE

All steps described in Sections 2.2-2.4 were implemented in Google Earth Engine (GEE) and executed at 30 m over the national forest domain. Analyses were conducted separately for three AOIs in Cyprus (Akamas-Area1, Stavrovouni-Area2, Machairas-Area3; Fig. 1), each anchored to a documented canopy-mortality event year (Area1: 2016; Area2: 2008; Area3: 2008) and its corresponding Landsat indicator (NBR for Areas 1–2; NDVI for Area3).

For each AOI, the reference mortality signature was quantified within the mapped confirmed mortality footprints using the baseline and change metrics defined in Section 2.3, while terrain, solar exposure, seasonal drought and lithology covariates (Section 2.4) were



Fig. 1. The morphological map of Cyprus, with selected study areas: Akamas (Area1), Stavrovouni (Area2), and Machairas (Area3).

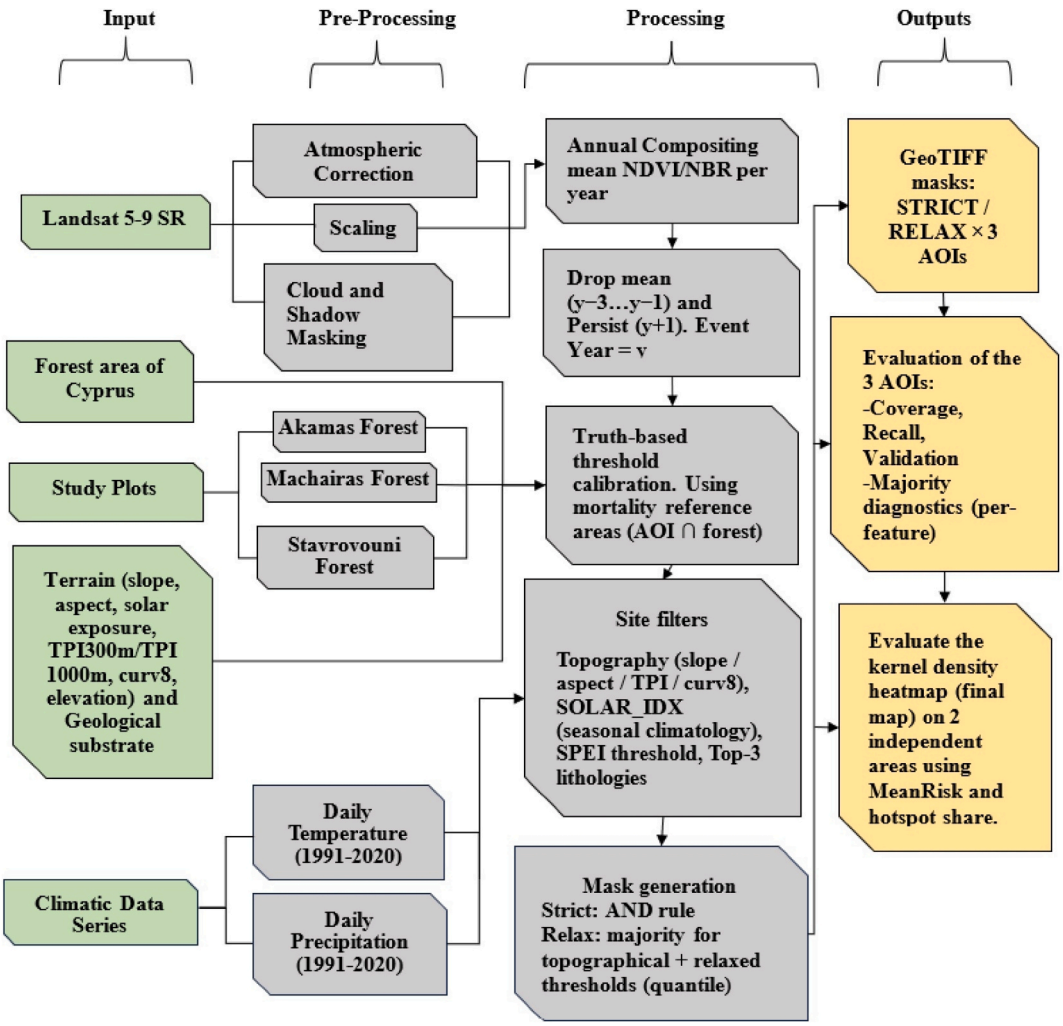


Fig. 2. Reference-anchored workflow for mapping drought-driven mortality risk hotspots. Topography: TPI300m/TPI1000m (relative position vs surrounding terrain at 300/1000 m + ridges, − valleys) and curv8 (8-neighbor curvature + convex, − concave).

summarized over the same footprint to parameterize reference-anchored similarity constraints. These constraints were then applied across the wider forest domain to delineate "where-else" forest pixels exhibiting environments consistent with the reference mortality setting (Fig. 2).

Workflow inputs/outputs and metrics are summarized in Supplementary Table S3, and all reproducibility scripts and parameters are provided in the Code Availability statement.

2.6. Threshold definition using quantile-based environmental envelopes

In a first step, we derived AOI-specific environmental thresholds for non-remote-sensing predictors. Continuous topographic variables (slope, TPI 300/1,000 m, curvature) were constrained using central quantile envelopes (0.05–0.95), whereas aspect, solar exposure, SPEI, and lithology were handled with variable-specific rules tailored to each AOI (Farber and Kadmon, 2003). Elevation was omitted due to collinearity with the seasonal SPEI constraint. Details of the threshold formulation and parameterization follow.

Aspect was treated as a circular variable to avoid discontinuities around 0°/360°. For each AOI, we computed the circular mean direction and circular dispersion of terrain aspect and used these statistics to define a reference-anchored orientation window. Pixels were retained when their aspect fell within a circular sector centered on the AOI circular mean, with sector width proportional to the AOI circular dispersion and scaled by a factor K (>1 in the current configuration) to widen the acceptable orientation range while remaining anchored to AOI-specific exposure.

A scaling factor of K = 1.5 was selected because it expands the aspect window to nearly the full directional range, preventing aspect from acting as an overly restrictive filter in heterogeneous terrain. This parameter is made available to end users for adjustment. The quantile bounds (0.05–0.95) were selected to exclude extreme outliers while retaining 90% of AOI physiographic conditions; narrower bounds (0.10–0.90) were found to reduce spatial coverage below the 60% reliability gate. The relax_drop_factor (0.60) and relax_persist_factor (0.50) were determined through iterative adjustment to maintain coverage and recall above the 60% reliability gate across all three AOIs, their sensitivity is reported in Supplementary Table S4.

Solar exposure was represented by a topo-aware `SOLAR_IDX` from 0 to 1, combining latitude, slope and aspect with the seasonal position of the sun. Monthly `SOLAR_IDX` layers were aggregated over April-September to obtain a seasonal mean. Within each AOI, `SOLAR_IDX` was summarized and an AOI-specific lower bound was defined as μ-σ; candidate pixels were required to exceed this minimum seasonal `SOLAR_IDX` (applied for Area1 and Area3 in the current configuration).

Meteorological drought was incorporated using the SPEI-12. For each event year, we derived an April-September mean SPEI-12 composite and imposed a spatially uniform threshold of SPEI $\leq$ -1.4 (derived empirically as the minimum seasonal SPEI value recorded across the confirmed mortality AOIs during the 2008 and 2016 events; Eliades et al., 2026) to restrict analyses to strongly water-limited conditions. This threshold is an adjustable parameter in the model, allowing end users to tighten or relax it depending on the target application.

Geological substrate (mapped lithology) was used as a constraint on substrate similarity. Each AOI was intersected with the national geological map, and the areal contribution of each lithological class was computed (pixel area). The three dominant lithological classes (top three by area) were retained.

In practice, the remaining continuous predictors were thresholded using AOI-specific empirical quantiles. For each AOI, we summarized the within-forest distributions of the relevant variables and used central quantile intervals to construct data-driven environmental envelopes (0.05–0.95 in the current configuration), thereby retaining the dominant range of conditions while excluding extreme outliers.

Quantiles provide a non-parametric, distribution-free summary that is robust to skew and outliers and assumes no normality, offering stable thresholds across heterogeneous terrain (Wasserman, 2004).

Here, quantile-based envelopes were applied to slope, topographic position indicators (TPI at 300 m and 1,000 m) and `curv8`. These envelopes were then combined with the variable-specific constraints described above to parameterize the final AOI-specific environmental similarity masks (Farber and Kadmon, 2003).

2.7. Evaluation and validation of final mortality-risk maps

Evaluation (*recall* and *spatial coverage*) of the final mortality-risk maps were performed at the AOI level, under the working assumption that each reference AOI represents a fully affected mortality footprint within the forest domain. The reference (hereafter the ground-truth mask, denoted truth) for all calculations was therefore defined as the AOI geometry intersected with the national 30-m forest mask (truth = AOI ∩ forest). All metrics were computed forest-only and within each AOI so that the reported values quantify how completely the final "where-else" masks recover the known affected footprint inside the corresponding AOI. To improve robustness and transferability of the mortality-resemblance signature across heterogeneous semi-arid terrain, we additionally applied a majority rule (Radoux and Bogaert, 2017).

Recall summarizes footprint recovery in pixel space. It was computed as the proportion of forest pixels inside the AOI that are also flagged by the predicted mask (pred ∩ truth divided by truth, where truth = AOI ∩ forest). Higher recall therefore indicates that the final mask captures a larger fraction of the affected AOI footprint (Maxwell et al., 2021).

Spatial coverage was quantified using an area-overlap metric within each AOI. Specifically, we calculated the fraction of the AOI's forest area that is covered by the predicted mask, using per-pixel area weights. This provides an area-based summary of footprint recovery that is less sensitive to small pixel-count differences along AOI boundaries and masking artefacts. Because the reference is defined as "AOI ∩ forest" on a fixed 30 m grid, recall (pixel-count recovery) and area-overlap spatial coverage (area-weighted recovery) are expected to be similar; we report both to provide parallel summaries that are differentially sensitive to minor boundary and masking effects (Maxwell et al., 2021).

Majority rule is used to increase the robustness and transferability (Chen et al., 2018) of the mortality-resemblance signature across heterogeneous semi-arid terrain. Because individual topographic predictors can be locally noisy or scale-sensitive (and some are partially redundant), requiring every constraint to be satisfied would make the envelope overly strict, fragment predictions and inflate false negatives when exported beyond the calibration AOI. By retaining pixels that satisfy at least 60% of the enabled terrain criteria, the method preserves the dominant physiographic "backbone" of the tree mortality setting while tolerating limited local departures, yielding more coherent and operationally useful high-risk screening maps.

To assess the transferability of spectral decline thresholds across sites, a leave-one-AOI-out cross-validation was conducted. In each fold, the event drop threshold was derived exclusively from the two remaining AOIs, and the held-out AOI was used for evaluation. Topographic envelopes were retained as AOI-specific by design, as they capture the physiographic template of each confirmed mortality footprint rather than a transferable threshold. Area3 (Machairas, *Q. alnifolia*) could not be held out under this design, as it is the sole NDVI-based calibration site; this constitutes an acknowledged limitation. Results are reported in Table 4.

2.8. Heatmap-derived intensity and polygon-level risk metrics

A heatmap-derived relative intensity index (HEAT; 0–1) was generated as a kernel density estimation (KDE)-based pressure surface for out-of-sample evaluation. This surface represents spatially smoothed concentration (i.e., proximity to and embedding within detected clusters),

highlighting potentially vulnerable areas (Silverman, 2018; Wand and Jones, 1994). Heatmap was summarized over the forested area within each target polygon using: (i) MeanRisk (%), defined as 100 × mean (HEAT) within the polygon, and (ii) Hotspot share (%), defined as the percentage of forested area exceeding high-intensity thresholds (HEAT $\geq$ 0.60 for high intensity and HEAT $\geq$ 0.80 for very high intensity/ hotspots).

For out-of-sample validation, the KDE smoothing kernel used a deliberately strict, small screen-space radius (2 km, $\sigma = r / 3$), yielding a conservative intensity surface with limited spatial diffusion. The smoothed surface was then rescaled to a relative intensity index (HEAT, 0–1) using a robust percentile stretch (P2-P98) and an optional gamma adjustment ($\gamma = 1.0$) prior to polygon-level summarization. This combination reduces overgeneralization beyond detected clusters and provides a more demanding basis for polygon-level risk assessment.

3. Results

3.1. Drought, topography and remotely sensed tree mortality in semi-arid regions

3.1.1. Data-driven physiographic, spectral and climatic characteristics of mortality footprints

The three mortality footprints span contrasting physiographic settings (Table 1). Akamas (*J. phoenicea*) is characterized by gentle to moderate south-southeast-facing slopes on ophiolitic substrate, with a mean NBR decline of −35.8% during the 2016 event. Machairas (*Q. alnifolia*) occupies steep east-northeast-facing high-elevation terrain on greywacke substrate, with a mean NDVI decline of −18.9% during the 2008 event. Stavrovouni (*P. brutia*) is confined to a narrow low-elevation belt on biocalcarenite substrate, with gentle northeast-facing slopes and a mean NBR decline of −16.9% during the 2008 event. Full threshold details are reported in Table 1.

3.2. Environmental envelopes of mortality-prone conditions across the semi-arid region footprints

Across the three semi-arid region footprints, the mortality-prone envelopes are reported for the dominant target species at each AOI: Akamas (*J. phoenicea*), Machairas (*Q. alnifolia*), and Stavrovouni (*P. brutia*) (Fig. 1). Site-level relaxed envelopes are presented for each AOI and are additionally synthesized in the composite Fig. 3, where the three region footprints are merged to produce a single layer of mortality-like "high-risk areas" for the overall study area experiencing elevated drought pressure.

The relaxed envelope parameters for each AOI are summarized in Table 2. Across all three sites, the relaxed configuration applies quantile bounds of 0.05–0.95, a majority rule (RELAX) with relax_K = 1.5, a

Table 2
Quantile-based environmental mortality thresholds across the three study areas.

Category	Variable	Area 1	Area 2	Area 3
Algorithm	mode	RELAX		
Quantile	Q_low	0.05	0.05	0.05
Quantile	Q_high	0.95	0.95	0.95
Drought (SPEI)	SPEI_thr_all	−1.40	−1.40	−1.40
Solar exposure	SOLAR_IDX_min	0.70	0.86	0.66
Solar exposure	SOLAR_IDX_max	0.99	0.99	0.99
Topography – TPI1000	TPI1000_min	21.69	−41.06	−63.80
Topography – TPI1000	TPI1000_max	85.49	–23.14	115.10
Topography – TPI300	TPI300_min	−12.55	−11.20	−66.16
Topography – TPI300	TPI300_max	30.25	5.82	40.38
Aspect	aspect_center_deg	145.21	21.07	74.07
Aspect	aspect_halfwidth_deg	80.35	87.94	37.37
Curvature	curv8_min	−100.00	−86.31	−100.00
Curvature	curv8_max	100.00	78.38	100.00
Slope	slope_min_deg	1	3	22
Slope	slope_max_deg	22	10	34
Geology	geology_codes	[34, 37, 10]	[5]	[34]

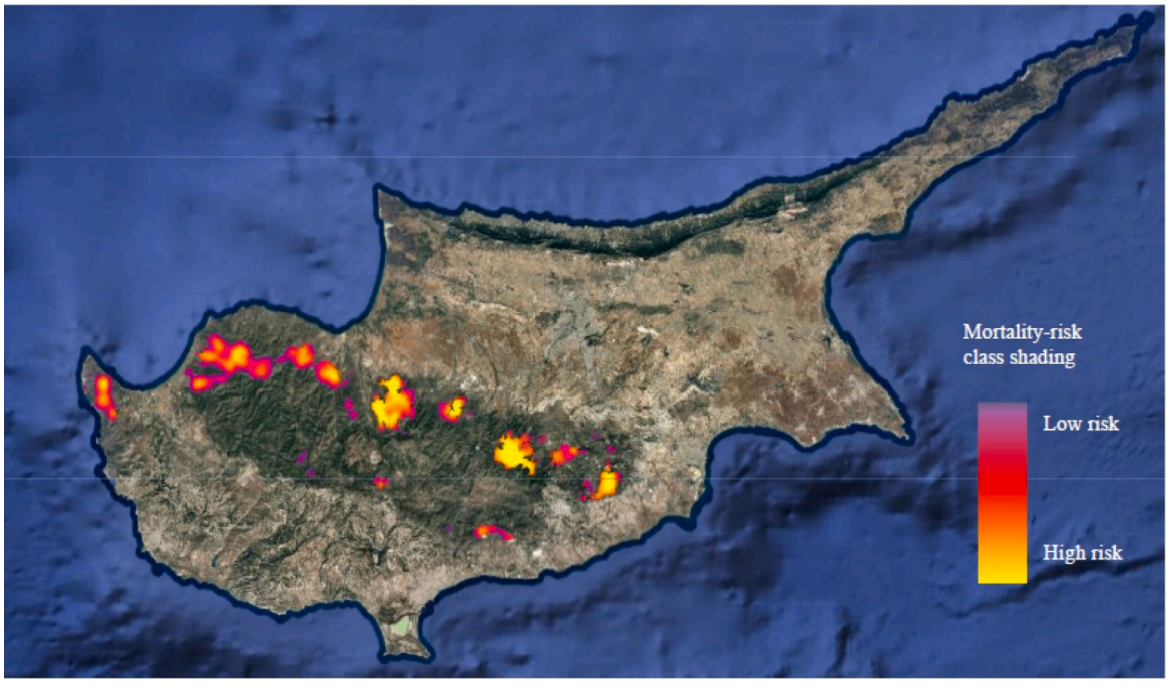


Fig. 3. High-risk area of mortality derived by merging the three AOI footprints: Akamas (*J. phoenicea*), Stavrovouni (*P. brutia*), and Machairas (*Q. alnifolia*), based on the relaxed environmental-envelope criteria.

uniform SPEI-12 drought gate of − 1.40, and spectral thresholds relaxed via relax_drop_factor = 0.60 and relax_persist_factor = 0.50. Site-specific differences are confined to the aspect envelope (centered on the AOI circular mean direction), the solar exposure threshold (reflecting contrasting topographic exposures), the geological substrate codes, and the topographic position ranges. Site-level relaxed envelopes are illustrated in Fig. 1 and synthesized in Fig. 3, where the three footprints are merged to produce a composite high-risk layer intended to support hotspot detection and monitoring prioritization across the study domain, rather than to estimate species-specific mortality rates or enable inter-species vulnerability comparisons.

3.3. Accuracy and assessment of mortality-prone mapping across sites

We evaluated the final mortality-prone mapping using the relaxed environmental envelope, which is the configuration used to generate the "resemblance-zone" masks.

As a descriptive measure of how broadly the relaxed envelope extends within the training AOIs, we quantified the fraction of forested area inside each AOI that is flagged by the relaxed mask (forest-only). Spatial coverage within the AOIs (Table 3) was 85.35% for Akamas (Area1), 71.38% for Stavrovouni (Area2) and 70.49% for Machairas (Area3). (For comparison, the strict configuration covered 0.00%, 1.22%, and 21.57% of forest area in Area1, Area2 and Area3, respectively.).

Leave-one-AOI-out cross-validation results are reported in Table 4. Under Fold 1 (Area1 held out, calibrated from Area2 only), coverage and recall remained at 85.35% and 100.00%, respectively, showing no degradation relative to the full model. Under Fold 2 (Area2 held out, calibrated from Area1 only), coverage and recall were 61.89% and 70.01%, both remaining above the 60% reliability gate.

As a percentage of pixels, we computed recall, defined as the number of true-positive pixels divided by the total number of reference mortality pixels. Under the relaxed configuration, recall (see Table 3) was 100.00% for Area1, 85.95% for Area2 and 67.62% for Area3 (under the strict configuration, recall was 11.71%, 4.16%, and 0.00% for Area1, Area2 and Area3, respectively).

3.4. Role of single topographic predictors in mortality risk

Under the *majority*-rule implementation of the relaxed environmental envelope (≥60% of enabled topographic criteria required per pixel), single-feature diagnostics show that slope, multi-scale topographic position (`TPI_300, TPI_1000`) and curvature (`curv8`) exert the strongest and most consistent control on the relaxed classification, whereas aspect is secondary and strongly site-dependent.

For Akamas (Area1), intersecting the relaxed mask with `SLOPE, TPI_300, TPI_1000` or `curv8` yields spatial coverage = 63.07–85.35% and captures most of the mortality reference within the AOI (recall = 76.29–79.71%). In contrast, `ASPECT` alone is weaker (spatial coverage = 65.63%, recall = 45.14%), indicating that the relaxed envelope is not primarily shaped by orientation constraints at this site (Table 5).

Stavrovouni (Area2): All five topographic predictors show moderate-to-strong alignment with the relaxed solution. Single-feature intersections give spatial coverage = 31.71–71.38% and recover 62.29–67.76% of mortality pixels (recall), with `curv8` yielding the highest recall (67.76%) and the highest spatial coverage (71.38%) (Table 5).

Machairas (Area3): `ASPECT` performs comparatively weaker in recall (spatial coverage = 70.50%, recall = 58.40%), while `SLOPE, TPI_300, TPI_1000` and `curv8` dominate: each reaches spatial coverage = 57.99–70.50% and recall = 68.43%. Overall, these diagnostics indicate that the relaxed "mortality-prone" envelope is driven mainly by terrain steepness, multi-scale topographic position and curvature (Table 5).

Table 3
Forest-only coverage/spatial coverage (% of AOI forest flagged) and recall (% of reference mortality pixels captured) under the relaxed envelope, by AOI.

Area	Spatial Coverage (% of forest AOI)	Recall (pixels)
Akamas	85.35	100.00
Stavrovouni	71.38	85.95
Machairas	70.49	67.62

Table 4
Leave-one-AOI-out cross-validation results for spectral threshold transferability.

Fold	Area	Species	Spatial Coverage (%)	Recall (%)
1	Akamas	*J. phoenicea*	85.35	100.00
2	Stavrovouni	*P. brutia*	61.89	70.01
3	Machairas	*Q. alnifolia*	N/A*	N/A*

* Sole NDVI-based calibration site; leave-one-out not applicable.

Table 5
Single-feature diagnostics for the RELAX majority-rule envelope (≥60% criteria satisfied per pixel) by AOI. Bold recall values indicate recall < 60%.

Area	Feature	Spatial Coverage %	Recall %
Akamas (Area 1)	`ASPECT`	65.63	45.14
	`SLOPE`	63.07	79.71
	`TPI_300`	71.17	76.29
	`TPI_1000`	73.14	76.29
	`CURV8`	85.35	79.71
Stavrovouni (Area 2)	`ASPECT`	61.23	62.29
	`SLOPE`	31.71	65.75
	`TPI_300`	51.03	64.50
	`TPI_1000`	60.58	64.50
	`CURV8`	71.38	67.76
Machairas (Area 3)	`ASPECT`	70.50	58.40
	`SLOPE`	67.29	68.43
	`TPI_300`	64.05	68.43
	`TPI_1000`	57.99	68.43
	`CURV8`	70.50	68.43

3.5. Evidence of transferability: Independent 2025 mortality captured by the event-anchored high-risk envelope

Beyond the within-AOI diagnostics, the relaxed reference-anchored framework provides an independent, post-calibration confirmation of transferability. Specifically, mortality polygons documented in 2025 at *Orkonta-Kambos tis Tsakistras* (OKT) (35.0739° N, 32.8257° E; WGS84) and *Pyrgos-Kambos tis Tsakistras* (PKT) (35.1056° N, 32.7511° E; WGS84) are fully contained within the spatial footprint that had already been delineated as high risk by envelopes calibrated exclusively on the 2008 and 2016 mortality signatures (Fig. 4). The mapped mortality-affected surface area was 214,333 m2 in OKT and 16,867 m2 in PKT. At the domain scale, the vulnerable areas (HEAT > 0) cover 18.88% of Cyprus's total forest area, while only 8.28% and 4.35% fall within the high-intensity classes HEAT ≥ 0.60 and HEAT ≥ 0.80, respectively, providing context for the within-polygon HEAT intensities reported below (Table 6).

The hydroclimatic context of the 2025 decline further aligns with the drought constraint embedded in the framework. The 12-month SPEI time series derived from the *Stavros tis Psokas* meteorological station (closest station to both independent mortality sites surveyed in 2025) indicates a prolonged drying phase initiating in 2021 and culminating in 2025, when SPEI dropped below −2 (extreme negative anomalies; Fig. 5).

This minimum exceeds the calibrated drought gate (SPEI ≤ -1.4) derived from the 2008 and 2016 mortality episodes, indicating that the 2025 event unfolded under hydroclimatic forcing that matches, and in several periods surpasses, the historical drought conditions associated

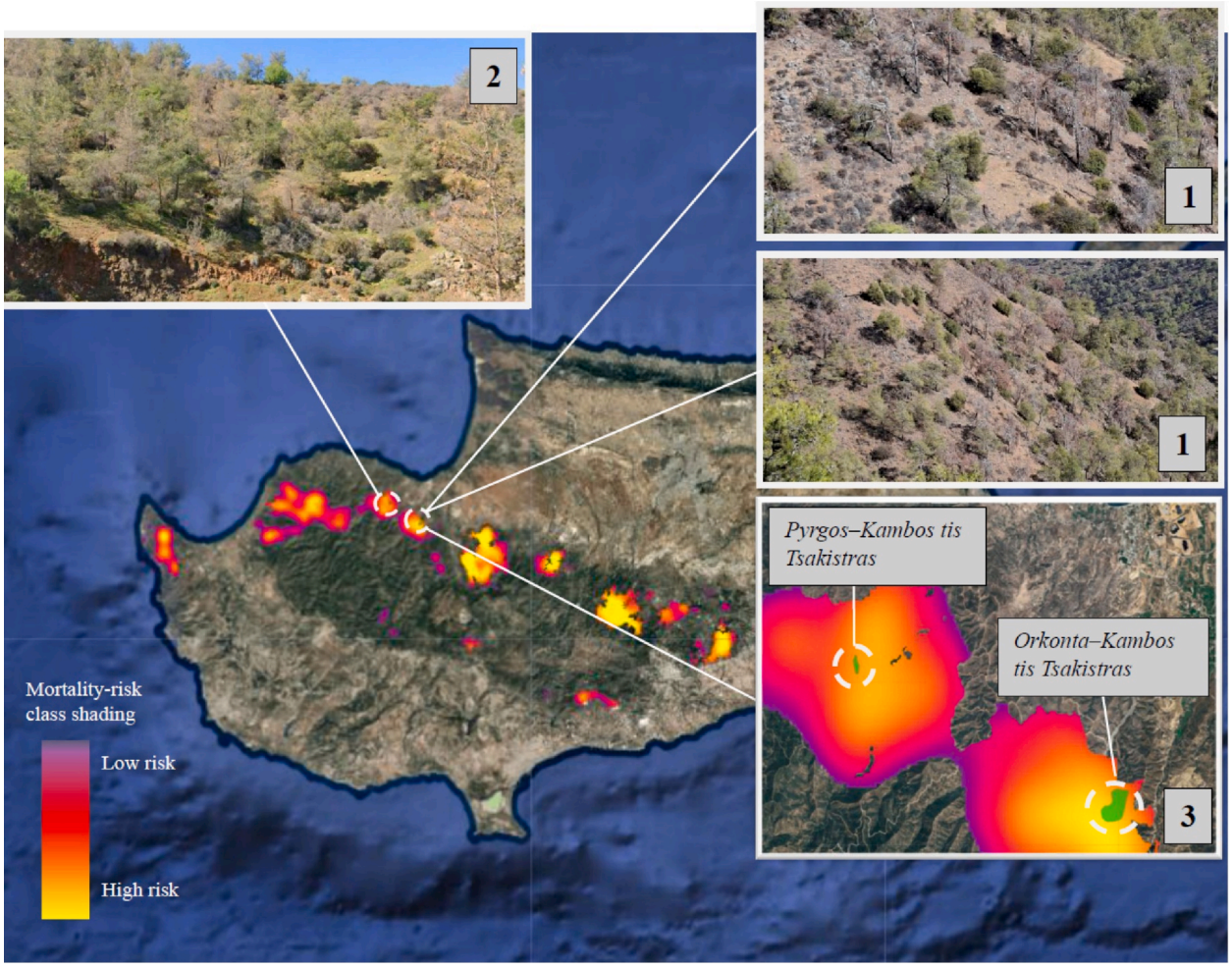


Fig. 4. Spatial footprint of the relaxed, reference-anchored high-risk envelope calibrated on the 2008 and 2016 mortality signatures, overlaid with polygons delineating the 2025 mortality-affected areas: (1) OKT, (2) PKT, and (3) dark-green polygons showing the mortality-affected areas mapped across the study region. (For interpretation of the references to colour in this figure legend, the reader is referred to the web version of this article.)

Table 6
Domain-scale coverage of HEAT classes over forested area: proportion of forest pixels with HEAT > 0, HEAT ≥ 0.60, and HEAT ≥ 0.80.

	High-intensity footprint (HEAT > 0)	High-intensity footprint (HEAT > 0.60)	High-intensity footprint (HEAT > 0.80)
Cyprus Forests (Area %)	18.88	8.28	4.35

with the reference mortality signatures (Fig. 5).

To independently corroborate the field observations using EO time series, we computed NBR over the 2025 affected zones and compared event-year behavior to the fixed pre-event baseline used for AOI signature extraction. The NBR series exhibits a sharp and unusually large negative excursion from 2021 to 2025 (i.e., a step-like spectral collapse), consistent with abrupt canopy degradation and mortality rather than transient stress (Fig. 6). Importantly, the timing of the strongest NBR decline coincides with the SPEI minimum (Fig. 5), supporting a coupled drought-canopy response during the 2025 episode.

3.6. Heatmap-derived relative risk within OKT and PKT

Heatmap (HEAT) metrics indicate that both 2025 mortality polygons are largely embedded within high-intensity hotspot clusters. PKT yielded a MeanRisk of 75.55%, with 82.69% of its forested area exceeding HEAT ≥ 0.60 and 0% exceeding HEAT ≥ 0.80. OKT exhibited a higher MeanRisk of 84.91%, with 83.50% of its forested area above HEAT ≥ 0.60 and 61.92% above HEAT ≥ 0.80 (Table 7). Overall, OKT shows consistently higher heatmap intensity than PKT, indicating stronger embedding within the highest-density hotspot core.

4. Discussion

4.1. Rationale for the ≥ 60% majority rule and sensitivity to threshold choice

The ≥ 60% majority rule provides a pragmatic balance between ecological plausibility and transferability in heterogeneous Mediterranean terrain. At 50%, pixels can pass with only half the physiographic constraints, yielding a permissive envelope where partially overlapping predictor combinations allow "easy" constraints to dominate, weakening interpretability and increasing the risk of mapping generic semi-arid forest conditions rather than the AOI mortality setting. Conversely, 70–80% becomes effectively intersection-like and overly sensitive to micro-site variability and single-predictor mismatches (e.g., exposure), driving systematic omission and, in some AOIs, coverage/recall <~50%. Thus, ≥60% is the most robust compromise (Shearman et al., 2019). To formally evaluate this choice, we conducted a sensitivity analysis across four majority-rule thresholds (20%, 40%, 60%, and 80%) and report coverage and recall for each AOI (Supplementary

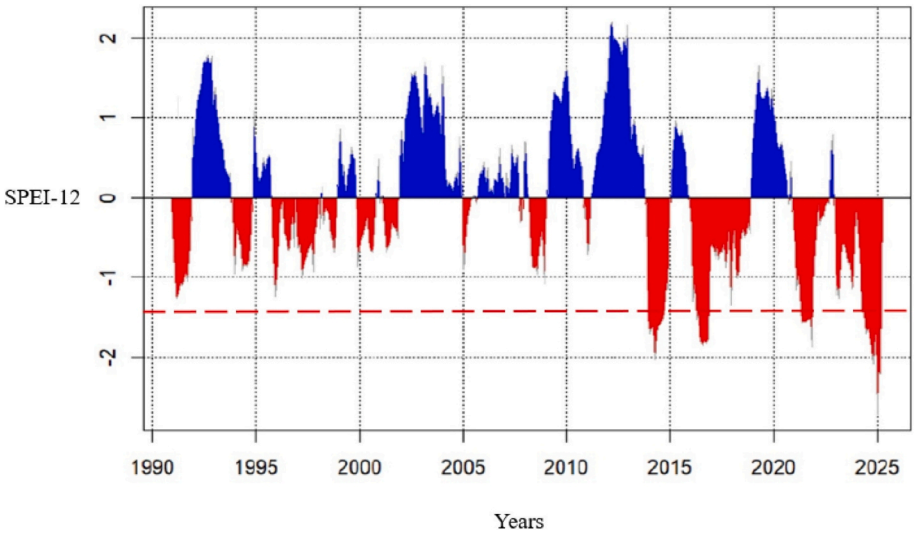


Fig. 5. Twelve-month SPEI time series from the *Stavros tis Psokas* meteorological station, indicating a prolonged drying phase culminating in severe drought conditions in 2025. Red dot line is the SPEI = -1.4. (For interpretation of the references to colour in this figure legend, the reader is referred to the web version of this article.)

Table S5). At 20% and 40%, coverage and recall improve marginally relative to 60% (e.g., Stavrovouni coverage: 79.77% vs. 71.38%; recall: 92.00% vs. 85.95%), but these thresholds require only one or two of five physiographic criteria to be satisfied, substantially weakening the discriminative power of the multi-factor signature. At 80%, performance degrades markedly, particularly in Stavrovouni (coverage: 50.12%; recall: 71.14%) and Machairas (recall: 57.59%), both falling below the 60% reliability gate proposed for actionable screening layers. This confirms that $\geq$ 60% represents the optimal balance between sensitivity and specificity across all three AOIs.

A complementary sensitivity analysis of the spectral relaxation parameters (relax_drop_factor and relax_persist_factor) is reported in Supplementary Table S4. The relax_persist_factor shows negligible sensitivity across the range 0.40–0.60, while increasing relax_drop_factor to 0.70 causes coverage to fall below the 60% reliability gate in two AOIs. The selected values are therefore the most conservative combination that maintains all AOIs above the reliability gate.

4.2. Relaxed resemblance zones: Recall and AOI spatial coverage

Using the relaxed environmental envelope, the final mortality-prone mapping showed strong alignment with the three calibration sites (Table 3). Spatial coverage and recall were consistently above the 60% reliability gate across all AOIs, indicating that the relaxed envelope spans broad physiographic space consistent with AOI conditions rather than being restricted to small idiosyncratic patches. Importantly, spatial coverage and recall are not expected to match numerically: spatial coverage quantifies the area fraction of AOI forests flagged by the model, whereas recall measures overlap against the mortality reference mask; the two metrics can diverge substantially depending on how the reference is defined and at what spatial support the overlap is computed.

We acknowledge that this evaluation is AOI-internal: the resemblance envelope is derived from and tested on the same footprints, which constitutes a form of circularity. The leave-one-AOI-out cross-validation partially addresses this by evaluating spectral threshold transferability across independent sites and species (Table 4). Both held-out AOIs retained coverage and recall above the 60% reliability gate (Fold 1: Area1, 85.35% and 100.00%; Fold 2: Area2, 61.89% and 70.01%), supporting the operational utility of the framework beyond the calibration footprint. The scope of this cross-validation should nonetheless be stated explicitly: it tests only the transferability of the spectral decline thresholds, while the AOI-specific topographic envelopes are retained by design and are therefore not cross-validated, and Area3 (the sole NDVI-based, weakest-performing site) is excluded because it cannot be held out. The validation consequently rests on two NBR-based folds and probes roughly half of the full pipeline rather than its topographic or NDVI components. The transferability evidence should be read accordingly.

4.3. A transferable drought-mortality signature confirmed in 2025

A key finding is that the AOI templates derived from the 2008 (Stavrovouni, Machairas) and 2016 (Akamas) events were not only internally coherent, but were also corroborated by two independent mortality occurrences in 2025 within areas prospectively flagged as priority locations. In both 2025 polygons, the screening signal was unambiguous: in PKT, 82.69% of the forested area exceeded HEAT $\geq$ 0.60, but 0% exceeded HEAT $\geq$ 0.80, with MeanRisk = 75.55%. In OKT, 83.50% of the forested area exceeded HEAT $\geq$ 0.60 and 61.93% exceeded HEAT $\geq$ 0.80, with MeanRisk = 84.91%. These values suggest that the 2025 occurrences were overwhelmingly concentrated within high-intensity hotspot zones, consistent with the hypothesis that reference-anchored physiographic similarity (quantile envelopes and a $\geq$ 60% majority rule), combined with the same process-consistent constraints used to define the 2008/2016 signatures (drought gating and decline persistence), can delineate areas where mortality-like outcomes may emerge under exceptionally strong drought forcing (SPEI). In this sense, the 2025 episode serves as an out-of-sample plausibility check, strengthening the interpretation of our outputs as actionable surveillance layers for prioritizing monitoring and targeted field verification rather than purely descriptive reconstructions of past events. To assess whether this co-occurrence is statistically meaningful, a binomial test was conducted. With 18.88% of Cyprus's total forest area flagged as high-risk (HEAT > 0), the probability that both independent 2025 sites would fall within the flagged zone by chance is $0.18882 \approx 0.036$ ($p < 0.05$), suggesting the overlap is unlikely to be random.

4.4. Implications for upscaling and "average thresholds" beyond the employed AOIs

The concurrent pattern of high within-AOI coverage and strong overlap with observed mortality (most notably in Areas 1–2) suggests that the relaxed physiographic envelope is well matched to its intended role: transferring a mortality-prone "resemblance" prior to landscapes

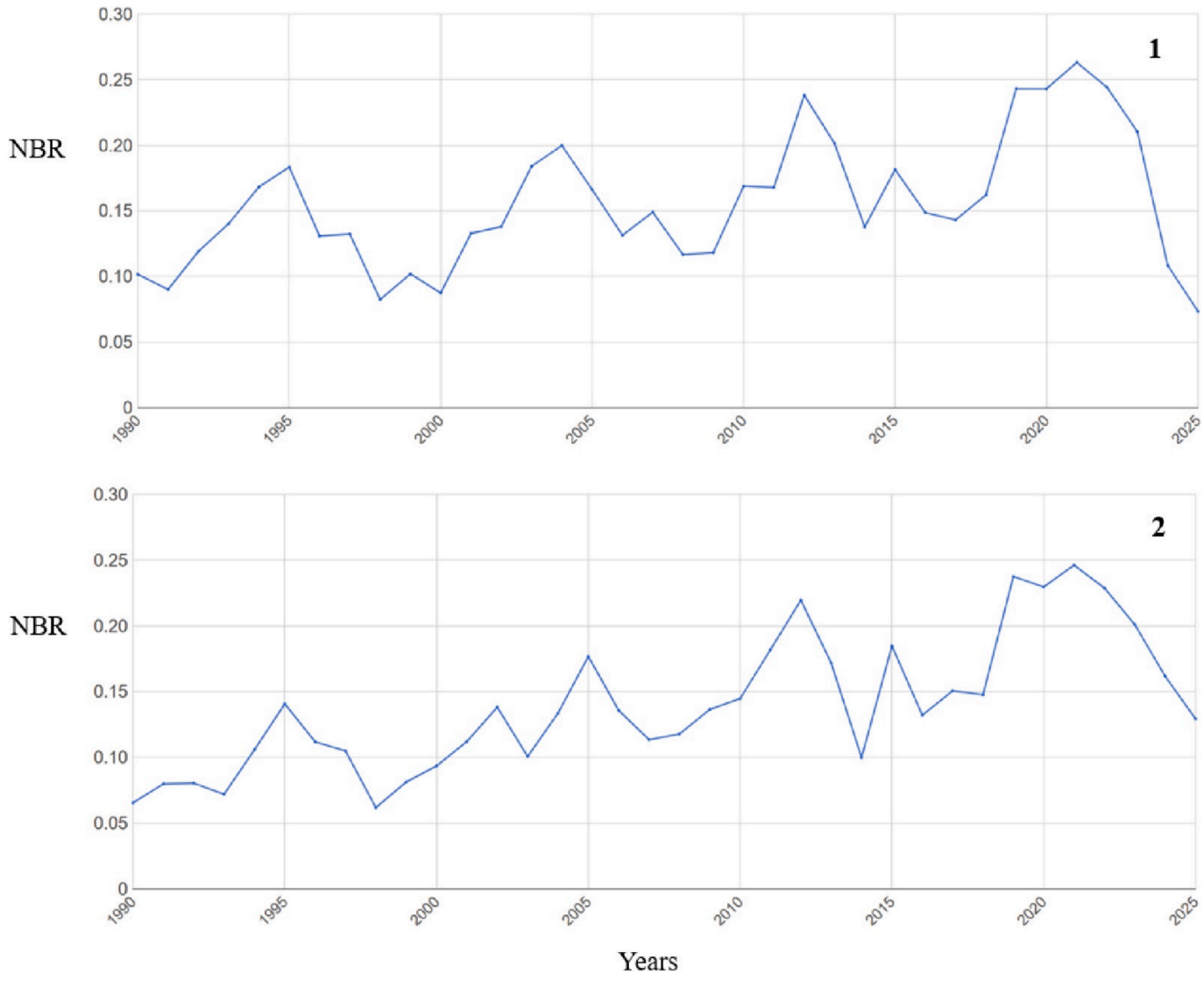


Fig. 6. NBR time series for (1) OKT and (2) PKT. Both sites show a sharp negative excursion culminating in 2025 relative to the pre-event baseline, consistent with rapid canopy degradation/mortality rather than transient stress.

Table 7
MeanRisk (%) is the mean HEAT value scaled to 0–100. High-intensity area (%) reports the proportion of forested area exceeding HEAT $\geq$ 0.60 and HEAT $\geq$ 0.80.

Affected Area	MeanRisk (%)	High-intensity area over 60% (%)	High-intensity area over 80% (%)
Pyrgos-Kambos tis Tsakistras	75.55	82.69	0
Orkonta-Kambos tis Tsakistras	84.91	83.50	61.92

beyond the calibration polygons, where stricter rule sets tend to be brittle and overly site-dependent (Guisan et al., 2017; Yates et al., 2018). This directly supports the broader workflow objective of iteratively expanding the model footprint, assimilating new regions, and converging on stable thresholds. In practice, slope, TPI, and curvature emerge as the most transferable constraints, whereas aspect should be applied more cautiously (e.g., through wider acceptance windows, reduced weighting, or conditional inclusion) when extending to morphologically distinct forest settings (Table 5).

4.5. Scope of inference, validation evidence, and steps toward stronger generalization

The framework is a reference-anchored screening layer that transfers a mortality-prone environmental signature from confirmed AOI footprints to prioritize surveillance and field checks, not a probabilistic mortality detector. Accordingly, we evaluate (i) whether relaxed majority-rule envelopes remain physiographically representative within AOIs and (ii) whether they recover event-consistent mortality reference pixels and associated recovery/persistence behavior. Independent evidence suggests transfer is operationally meaningful: mortality-like episodes documented in 2025 occurred within areas pre-flagged as high risk using signatures derived from the 2008/2016 events (Section 3.5), and heatmap diagnostics support spatial concordance with affected polygons. Robust forest-wide omission/commission estimates would require spatially exhaustive independent inventories, which are rarely available; where they exist, the workflow supports hold-out and spatially blocked validation. Expanding the reference library and conducting sensitivity analyses (thresholds/quantiles and key preprocessing choices) would further strengthen generality and uncertainty characterization (Mbogga et al., 2010; Wiens et al., 2009). We acknowledge that two independent sites constitute a plausibility check rather than a

statistically rigorous validation, and that broader applicability across the Mediterranean region would require a larger independent sample spanning diverse forest types, climate regimes, and mortality drivers. Acquiring such a dataset remains a priority for future work. A formal commission rate cannot be computed because the national forest mask contains no spatially exhaustive record of confirmed healthy stands, undetected mortality events, management interventions, and natural disturbances may occur throughout the domain, making it impossible to define true negatives with confidence. The 18.88% domain-wide flag rate and binomial test ($p \approx 0.036$) therefore represent the most rigorous indirect assessment possible given available data. Pooling three species with contrasting drought-response physiology (*J. phoenicea, P. brutia, Q. alnifolia*) is a deliberate methodological choice grounded in two considerations. First, the framework targets the landscape physiographic and hydroclimatic template that predisposes forest stands to drought stress, rather than species-specific mortality thresholds. Second, broadleaved species (*Q. alnifolia*) are known to exhibit delayed physiological responses to drought (Eliades et al., 2026), meaning that the composite map captures primarily the drought signal acting on coniferous species while the broadleaved AOI contributes physiographic context. The resulting composite layer therefore reflects the spatial imprint of drought forcing across contrasting forest types rather than a species-specific mortality model. This interpretation is further supported by the leave-one-AOI-out results (Table 4), which demonstrate successful threshold transferability across species with distinct physiology, suggesting that landscape position and drought severity are primary controls on mortality susceptibility in this semi-arid context.

4.6. Management implications for proactive forest protection

From an operational management perspective, the mapped "resemblance zones" can be used as a preventive risk-management layer that translates susceptibility into concrete, field-ready action rather than a *post hoc* description of tree mortality. This represents a practical shift from broad surveillance to targeted intervention: when seasonal drought alerts (e.g., negative SPEI anomalies) coincide with remotely sensed stress consistent with the reference signatures (event-year spectral decline relative to baseline, with post-event persistence), managers can trigger rapid ground checks focused within the most mortality-prone terrain units. A proposed Operational Decision Flow of the above managerial steps is outlined in Fig. 7.

Because these "resemblance zones" are shaped by stable physiographic controls that repeatedly predispose stands to water limitation, managers can prioritize targeted actions to reduce drought stress and prevent secondary mortality. Key measures include light, selective thinning in overstocked patches to lower competition for water (Chagnon et al., 2025), targeted understory reduction (shrubs/grass) where it is suppressing regeneration or intensifying drought stress (Lecomte et al., 2022), protecting soil function by minimizing compaction and erosion while retaining litter and woody debris to sustain infiltration and root-zone moisture (Orfánus et al., 2021), and intensified monitoring with rapid containment of drought-amplified insects and pathogens. After confirmed events, the same risk layer can guide restoration by prioritizing assisted natural regeneration and, where planting is needed, selecting locally suitable provenances and drought-tolerant species mixtures matched to site conditions to strengthen resilience to recurrent drought extremes (Fremout et al., 2022).

4.7. Transferability of the framework for climate-risk screening across regions

A central advantage of the framework described in the present research is that it provides a transferable route to national-scale prioritization in regions where only a limited number of mortality episodes are well documented. The reference-anchored envelope-based susceptibility model is designed for national-to-regional scaling because calibration relies on a small set of documented AOIs, while prediction is executed across a forest mask using globally available EO (Earth Observation) inputs and AOI-specific non-parametric envelopes rather than site-tuned parametric models. Additional tree mortality episodes can be incorporated as new AOI signatures, expanding a library of transferable resemblance priors. This enables rapid, repeatable redeployment across administrative units to support drought-time surveillance and prioritization. Anchoring on a small set of confirmed reference AOIs, the method generalizes via physiographic similarity-using broad quantile envelopes combined under a majority rule, optionally constrained by solar exposure and geological substrate. In parallel, it uses dynamic stress fingerprints (event-year spectral decline and post-event persistence) to separate "*where vulnerability is structurally likely*" from "*when vulnerability is activated*". This is particularly relevant under rapid climate change, where drought extremes are intensifying and shifting in space: when an anomalous SPEI episode occurs, the framework converts a generic national drought signal into geographically explicit predictions of which forest areas are most likely to approach mortality thresholds. The result is an actionable, reproducible risk atlas built from globally available satellite and climate datasets, enabling cross-country adoption for targeted surveillance, earlier intervention, and more efficient allocation of limited management resources.

5. Conclusion

In this study, we developed and tested a reference-anchored, envelope-based susceptibility model that transfers drought-mortality signatures from confirmed mortality footprints to broader semi-arid forest landscapes by coupling physiographic similarity with event-consistent spectral decline and post-event persistence. Applied to three

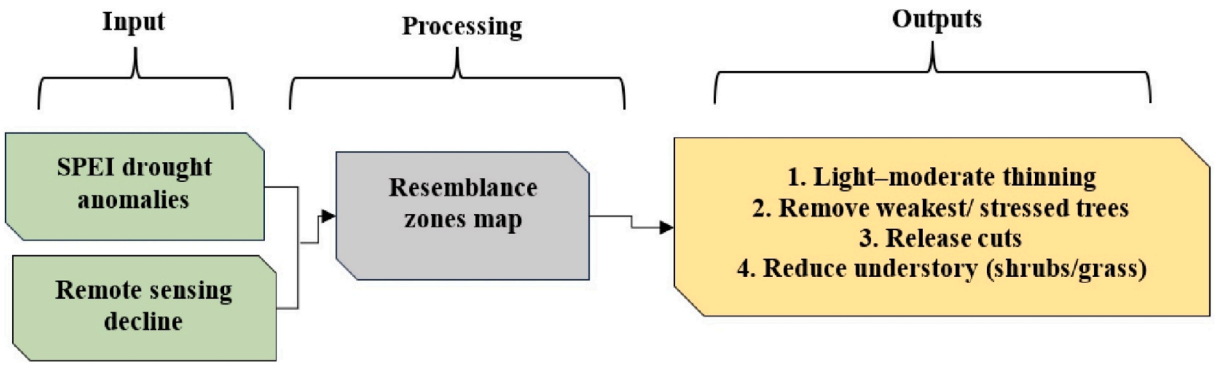


Fig. 7. Operational decision flow linking drought alerts and remote-sensing stress signals to targeted field inspections and interventions within mapped "resemblance zones".

contrasting AOIs in Cyprus, the relaxed resemblance configuration recovered a substantial fraction of reference mortality pixels while maintaining within-AOI forest representativeness, supporting its use as a transferable screening layer for surveillance rather than a definitive mortality detection tool.

Out-of-sample confirmation from two independently documented 2025 mortality sites (both of which had been pre-flagged by the 2008/2016 AOI signatures) provides encouraging support for the operational transferability of the framework under extreme drought forcing. A.

The method leverages globally available Earth observation covariates, making it well suited to the Eastern Mediterranean and readily transferable to other semi-arid regions. New AOIs with confirmed mortality footprints can be incorporated to derive locally tailored signatures, extending the framework's applicability across diverse forest-climate contexts. Future work should focus on expanding the reference library, incorporating species-specific drought-response thresholds, and conducting independent landscape-scale validation to further strengthen generality.

CRediT authorship contribution statement

Filippos Eliades: Writing – original draft, Validation, Software, Methodology, Formal analysis, Data curation. **Dimitrios Sarris:** Writing – review & editing. **Felix Bachofer:** Writing – review & editing, Supervision. **Silas Michaelides:** Writing – review & editing. **Chris Danezis:** Writing – review & editing, Supervision, Conceptualization. **Diofantos Hadjimitsis:** Writing – review & editing, Supervision, Funding acquisition.

Declaration of Generative AI and AI-assisted technologies in the writing process

During the preparation of this work the authors used ChatGPT and Grammarly to refine and condense the text. After using this model/service, the authors reviewed and edited the content as needed, and take full responsibility for the content of the publication.

Code availability

The Google Earth Engine source code developed for this study is archived at Zenodo (Eliades, 2026; https://doi.org/10.5281/zenodo.20154761) under a CC BY-NC 4.0 license.

Funding

This research was funded by the 'EXCELSIOR' project (European Union's Horizon 2020 Research and Innovation Programme), grant number "857510".

Declaration of competing interest

The authors declare that they have no known competing financial interests or personal relationships that could have appeared to influence the work reported in this paper.

Acknowledgements

The authors acknowledge the "EXCELSIOR": ERATOSTHENES: Excellence Research Centre for Earth Surveillance and Space-Based Monitoring of the Environment H2020 Widespread Teaming project (**www.excelsior2020.eu**, accessed on 1 July 2024). The "EXCELSIOR" project has received funding from the European Union's Horizon 2020 Research and Innovation Programme under Grant Agreement No 857510 from the Government of the Republic of Cyprus through the Directorate General for the European Programmes, Coordination and Development, and the Cyprus University of Technology.

Appendix A. Supplementary data

Supplementary data to this article can be found online at https://doi.org/10.1016/j.jag.2026.105609.

Data availability

The datasets generated during this study (AOI geometries, mortality reference masks, AOI-derived threshold tables, and exported mortality-resemblance raster layers) will be made publicly available upon acceptance via a trusted repository (DOI to be provided in the final published version). All third-party input datasets are publicly available and accessed via Google Earth Engine: Landsat Collection 2 Level-2 (USGS), Copernicus DEM GLO-30 (ESA), CSIC SPEI v2.10, national forest mask, and geological substrate layers.

References

Allen, C.D., Macalady, A.K., Chenchouni, H., Bachelet, D., McDowell, N., Vennetier, M., Kitzberger, T., Rigling, A., Breshears, D.D., Hogg, E.H. (Ted), Gonzalez, P., Fensham, R., Zhang, Z., Castro, J., Demidova, N., Lim, J.-H., Allard, G., Running, S.W., Semerci, A., Cobb, N., 2010. A global overview of drought and heat-induced tree mortality reveals emerging climate change risks for forests. For. Ecol. Manag. 259, 660–684. https://doi.org/10.1016/j.foreco.2009.09.001.

Amatulli, G., Domisch, S., Tuanmu, M.-N., Parmentier, B., Ranipeta, A., Malczyk, J., Jetz, W., 2018. A suite of global, cross-scale topographic variables for environmental and biodiversity modeling. Sci. Data 5, 180040. https://doi.org/10.1038/sdata.2018.40.

Baguskas, S.A., Peterson, S.H., Bookhagen, B., Still, C.J., 2014. Evaluating spatial patterns of drought-induced tree mortality in a coastal California pine forest. For. Ecol. Manag. 315, 43–53. https://doi.org/10.1016/j.foreco.2013.12.020.

Banskota, A., Kayastha, N., Falkowski, M.J., Wulder, M.A., Froese, R.E., White, J.C., 2014. Forest monitoring using Landsat Time Series Data: a Review. Can. J. Remote. Sens. 40, 362–384. https://doi.org/10.1080/07038992.2014.987376.

Breshears, D.D., Cobb, N.S., Rich, P.M., Price, K.P., Allen, C.D., Balice, R.G., Romme, W. H., Kastens, J.H., Floyd, M.L., Belnap, J., Anderson, J.J., Myers, O.B., Meyer, C.W., 2005. Regional vegetation die-off in response to global-change-type drought. PNAS 102, 15144–15148. https://doi.org/10.1073/pnas.0505734102.

Camera, C., Zomeni, Z., Noller, J.S., Zissimos, A.M., Christoforou, I.C., Bruggeman, A., 2017. A high resolution map of soil types and physical properties for Cyprus: a digital soil mapping optimization. Geoderma 285, 35–49. https://doi.org/10.1016/j.geoderma.2016.09.019.

Carnicer, J., Coll, M., Ninyerola, M., Pons, X., Sánchez, G., Peñuelas, J., 2011. Widespread crown condition decline, food web disruption, and amplified tree mortality with increased climate change-type drought. PNAS 108, 1474–1478. https://doi.org/10.1073/pnas.1010070108.

Chagnon, C., Dumont, S., Morin-Bernard, A., Jactel, H., Achim, A., Moreau, G., 2025. Potential of thinning to increase forest resilience and resistance to drought, pest, windstorm and fire: a meta-analysis. For. Ecol. Manag. 590, 122788. https://doi.org/10.1016/j.foreco.2025.122788.

Chen, Y., Zhou, Y., Ge, Y., An, R., Chen, Yu., 2018. Enhancing Land Cover Mapping through Integration of Pixel-based and Object-based Classifications from Remotely Sensed Imagery. Remote Sens. 10, 77. https://doi.org/10.3390/rs10010077.

Copernicus Data Space Ecosystem, 2026. Copernicus DEM - Global and European Digital Elevation Model [WWW Document]. URL https://dataspace.copernicus.eu/explore-data/data-collections/copernicus-contributing-missions/collections-description/COP-DEM.

De Marzo, T., Pflugmacher, D., Baumann, M., Lambin, E.F., Gasparri, I., Kuemmerle, T., 2021. Characterizing forest disturbances across the Argentine Dry Chaco based on Landsat time series. Int. J. Appl. Earth Obs. Geoinf. 98, 102310. https://doi.org/10.1016/j.jag.2021.102310.

Dorman, M., Svoray, T., Perevolotsky, A., Moshe, Y., Sarris, D., 2015. What determines tree mortality in dry environments? a multi-perspective approach. Ecol. Appl. 25, 1054–1071. https://doi.org/10.1890/14-0698.1.

Eliades, F., Sarris, D., Bachofer, F., Michaelides, S., Hadjimitsis, D., 2024. Understanding tree Mortality patterns: a Comprehensive Review of Remote Sensing and Meteorological Ground-based Studies. Forests 15, 1357. https://doi.org/10.3390/f15081357.

Eliades, F., Sarris, D., Bachofer, F., Michaelides, S., Danezis, C., Hadjimitsis, D., 2026. Forests in a semi-arid climate die with a memory: satellite signals predict forest mortality years after drought. J. for. Res. 37, 79. https://doi.org/10.1007/s11676-026-02016-z.

Farber, O., Kadmon, R., 2003. Assessment of alternative approaches for bioclimatic modeling with special emphasis on the Mahalanobis distance. Ecol. Model. 160, 115–130. https://doi.org/10.1016/S0304-3800(02)00327-7.

Fremout, T., Thomas, E., Taedoumg, H., Briers, S., Gutiérrez-Miranda, C.E., Alcázar-Caicedo, C., Lindau, A., Mounmemi Kpoumie, H., Vinceti, B., Kettle, C., Ekué, M., Atkinson, R., Jalonen, R., Gaisberger, H., Elliott, S., Brechbühler, E., Ceccarelli, V., Krishnan, S., Vacik, H., Wiederkehr-Guerra, G., Salgado-Negret, B., González, M.A., Ramírez, W., Moscoso-Higuita, L.G., Vásquez, Á., Cerrón, J., Maycock, C., Muys, B., 2022. Diversity for Restoration (D4R): Guiding the selection of tree species and seed

sources for climate-resilient restoration of tropical forest landscapes. J. Appl. Ecol. 59, 664–679. https://doi.org/10.1111/1365-2664.14079.
Gea-Izquierdo, G., Viguera, B., Cabrera, M., Cañellas, I., 2014. Drought induced decline could portend widespread pine mortality at the xeric ecotone in managed mediterranean pine-oak woodlands. For. Ecol. Manag. 320, 70–82. https://doi.org/10.1016/j.foreco.2014.02.025.
Guan, H., Dong, X., Yan, G., Searls, T., Bourque, C.-P.-A., Meng, F.-R., 2021. Conditional inference trees in the assessment of tree mortality rates in the transitional mixed forests of Atlantic Canada. PLoS ONE 16, e0250991. https://doi.org/10.1371/journal.pone.0250991.
Guisan, A., Thuiller, W., Zimmermann, N.E., 2017. Habitat Suitability and Distribution Models: With Applications in R, 1st ed. Cambridge University Press. https://doi.org/10.1017/9781139028271.
Gustafson, E.J., Sturtevant, B.R., 2013. Modeling Forest Mortality Caused by Drought stress: Implications for climate Change. Ecosystems 16, 60–74. https://doi.org/10.1007/s10021-012-9596-1.
Hawbaker, T.J., Vanderhoof, M.K., Beal, Y.-J., Takacs, J.D., Schmidt, G.L., Falgout, J.T., Williams, B., Fairaux, N.M., Caldwell, M.K., Picotte, J.J., Howard, S.M., Stitt, S., Dwyer, J.L., 2017. Mapping burned areas using dense time-series of Landsat data. Remote Sens. Environ. 198, 504–522. https://doi.org/10.1016/j.rse.2017.06.027.
Huesca, M., Ustin, S.L., Shapiro, K.D., Boynton, R., Thorne, J.H., 2021. Detection of drought-induced blue oak mortality in the Sierra Nevada Mountains. California. Ecosphere 12, e03558. https://doi.org/10.1002/ecs2.3558.
Julio Camarero, J., Gazol, A., Sangüesa-Barreda, G., Cantero, A., Sánchez-Salguero, R., Sánchez-Miranda, A., Granda, E., Serra-Maluquer, X., Ibáñez, R., 2018. Forest growth responses to Drought at Short- and Long-Term Scales in Spain: Squeezing the stress memory from tree Rings. Front. Ecol. Evol. 6, 9. https://doi.org/10.3389/fevo.2018.00009.
Lecomte, X., Paulo, J.A., Tomé, M., Veloso, S., Firmino, P.N., Faias, S.P., Caldeira, M.C., 2022. Shrub understorey clearing and drought affects water status and growth of juvenile *Quercus suber* trees. For. Ecol. Manag. 503, 119760. https://doi.org/10.1016/j.foreco.2021.119760.
Ma, Q., Su, Y., Niu, C., Ma, Q., Hu, T., Luo, X., Tai, X., Qiu, T., Zhang, Y., Bales, R.C., Liu, L., Kelly, M., Guo, Q., 2023. Tree mortality during long-term droughts is lower in structurally complex forest stands. Nat. Commun. 14, 7467. https://doi.org/10.1038/s41467-023-43083-8.
Maxwell, A.E., Warner, T.A., Guillén, L.A., 2021. Accuracy Assessment in Convolutional Neural Network-based Deep Learning Remote Sensing Studies—Part 1: Literature Review. Remote Sens. 13, 2450. https://doi.org/10.3390/rs13132450.
Mbogga, M.S., Wang, X., Hamann, A., 2010. Bioclimate envelope model predictions for natural resource management: dealing with uncertainty. J. Appl. Ecol. 47, 731–740. https://doi.org/10.1111/j.1365-2664.2010.01830.x.
McLaughlin, B.C., Blakey, R., Weitz, A.P., Feng, X., Brown, B.J., Ackerly, D.D., Dawson, T.E., Thompson, S.E., 2020. Weather underground: Subsurface hydrologic processes mediate tree vulnerability to extreme climatic drought. Glob. Change Biol. 26, 3091–3107. https://doi.org/10.1111/gcb.15026.
Nardini, A., Tomasella, M., Di Bert, S., 2024. Bedrock: the hidden water reservoir for trees challenged by drought. Trees 38, 1–11. https://doi.org/10.1007/s00468-023-02482-6.
Orfánus, T., Zvala, A., Čierniková, M., Stojkovová, D., Nagy, V., Dlapa, P., 2021. Peculiarities of Infiltration Measurements in Water-Repellent Forest Soil. Forests 12, 472. https://doi.org/10.3390/f12040472.
Paz-Kagan, T., Brodrick, P.G., Vaughn, N.R., Das, A.J., Stephenson, N.L., Nydick, K.R., Asner, G.P., 2017. What mediates tree mortality during drought in the southern Sierra Nevada? Ecol. Appl. 27, 2443–2457. https://doi.org/10.1002/eap.1620.
Radoux, J., Bogaert, P., 2017. Good Practices for Object-based Accuracy Assessment. Remote Sens. 9, 646. https://doi.org/10.3390/rs9070646.
Regos, A., Gagne, L., Alcaraz-Segura, D., Honrado, J.P., Domínguez, J., 2019. Effects of species traits and environmental predictors on performance and transferability of ecological niche models. Sci. Rep. 9, 4221. https://doi.org/10.1038/s41598-019-40766-5.
Rodríguez Paulino, E., Schlerf, M., Röder, A., Stoffels, J., Udelhoven, T., 2024. Forest disturbance characterization in the era of earth observation big data: a mapping review. Int. J. Appl. Earth Obs. Geoinf. 128, 103755. https://doi.org/10.1016/j.jag.2024.103755.
Salekin, S., Mason, E.G., Morgenroth, J., Bloomberg, M., Meason, D.F., 2019. Modelling the effect of Microsite Influences on the growth and Survival of Juvenile Eucalyptus globoidea (Blakely) and Eucalyptus bosistoana (F. Muell) in New Zealand. Forests 10, 857. https://doi.org/10.3390/f10100857.
Sánchez-Salguero, R., Camarero, J.J., 2020. Greater sensitivity to hotter droughts underlies juniper dieback and mortality in Mediterranean shrublands. Sci. Total Environ. 721, 137599. https://doi.org/10.1016/j.scitotenv.2020.137599.
Sang, Y., Tian, F., Jin, H., Cai, Z., Feng, L., Dou, Y., Eklundh, L., 2024. Assessing topographic effects on forest responses to drought with multiple seasonal metrics from Sentinel-2. Int. J. Appl. Earth Obs. Geoinf. 128, 103789. https://doi.org/10.1016/j.jag.2024.103789.
Sarris, D., Christodoulakis, D., 2024. Topographic and climatic effects on *Pinus halepensis* s.l. growth at its drought tolerance margins under climatic change. J. for. Res. 35, 102. https://doi.org/10.1007/s11676-024-01755-1.
Schwantes, A.M., Parolari, A.J., Swenson, J.J., Johnson, D.M., Domec, J., Jackson, R.B., Pelak, N., Porporato, A., 2018. Accounting for landscape heterogeneity improves spatial predictions of tree vulnerability to drought. New Phytol. 220, 132–146. https://doi.org/10.1111/nph.15274.
Schwartz, N.B., Feng, X., Muscarella, R., Swenson, N.G., Umaña, M.N., Zimmerman, J.K., Uriarte, M., 2020. Topography and Traits Modulate tree Performance and Drought Response in a Tropical Forest. Front. for. Glob. Change 3, 596256. https://doi.org/10.3389/ffgc.2020.596256.
Shearman, T.M., Varner, J.M., Hood, S.M., Cansler, C.A., Hiers, J.K., 2019. Modelling post-fire tree mortality: can random forest improve discrimination of imbalanced data? Ecol. Model. 414, 108855. https://doi.org/10.1016/j.ecolmodel.2019.108855.
Silverman, B.W., 2018. Density Estimation for Statistics and Data Analysis, 1st ed. Routledge. https://doi.org/10.1201/9781315140919.
Tucker, C.J., 1979. Red and photographic infrared linear combinations for monitoring vegetation. Remote Sens. Environ. 8, 127–150. https://doi.org/10.1016/0034-4257(79)90013-0.
Vicente-Serrano, S.M., Beguería, S., López-Moreno, J.I., 2010. A Multiscalar Drought Index Sensitive to Global Warming: the Standardized Precipitation Evapotranspiration Index. J. Clim. 23, 1696–1718. https://doi.org/10.1175/2009JCLI2909.1.
Wand, M.P., Jones, M.C., 1994. Kernel Smoothing, 0 ed. Chapman and Hall/CRC. https://doi.org/10.1201/b14876.
Wasserman, L., 2004. All of Statistics: A Concise Course in Statistical Inference, Springer Texts in Statistics. Springer New York, New York, NY. https://doi.org/10.1007/978-0-387-21736-9.
Wiens, J.A., Stralberg, D., Jongsomjit, D., Howell, C.A., Snyder, M.A., 2009. Niches, models, and climate change: Assessing the assumptions and uncertainties. Proc. Natl. Acad. Sci. u.s.a. 106, 19729–19736. https://doi.org/10.1073/pnas.0901639106.
Yates, K.L., Bouchet, P.J., Caley, M.J., Mengersen, K., Randin, C.F., Parnell, S., Fielding, A.H., Bamford, A.J., Ban, S., Barbosa, A.M., Dormann, C.F., Elith, J., Embling, C.B., Ervin, G.N., Fisher, R., Gould, S., Graf, R.F., Gregr, E.J., Halpin, P.N., Heikkinen, R.K., Heinänen, S., Jones, A.R., Krishnakumar, P.K., Lauria, V., Lozano-Montes, H., Mannocci, L., Mellin, C., Mesgaran, M.B., Moreno-Amat, E., Mormede, S., Novaczek, E., Oppel, S., Ortuño Crespo, G., Peterson, A.T., Rapacciuolo, G., Roberts, J.J., Ross, R.E., Scales, K.L., Schoeman, D., Snelgrove, P., Sundblad, G., Thuiller, W., Torres, L.G., Verbruggen, H., Wang, L., Wenger, S., Whittingham, M.J., Zharikov, Y., Zurell, D., Sequeira, A.M.M., 2018. Outstanding challenges in the Transferability of Ecological Models. Trends Ecol. Evol. 33, 790–802. https://doi.org/10.1016/j.tree.2018.08.001.